Dynamic Modeling of a Novel Microfluidic Channel Angular Accelerometer

H. JURGENS WOLFAARDT
P. STEPHAN HEYNS
Dynamic Systems Group, University of Pretoria, South Africa (stephan.heyns@up.ac.za)

(Received 5 October 2006; accepted 13 February 2007)

Abstract: The angular accelerometer is a versatile inertial instrument, with applications ranging from vehicle stabilization to navigation and satellite pointing. A novel angular accelerometer is proposed, which is able to improve on contemporary angular accelerometers and micro-electromechanical system gyroscopes. The sensor consists of micro-machined spiral channels, fabricated on multiple wafers and used to construct a spiral-helix fluid column that generates high pressure during angular acceleration round the sensitive axis. The two ends of the fluid column are joined at a central measurement chamber, where a diaphragm-based pressure transducer produces a signal proportional to the angular acceleration applied. This article presents the dynamics of the sensor, and then investigates its potential. A discrete multiple-degree-of-freedom model simulates pressure generation and propagation, and was verified experimentally. Channel flow is simulated by means of a model derived from Szymanski's theory of unsteady laminar flow. The pressure transducer diaphragm model is based on linear flat plate theory. The sensor theory is synthesized in a linear sensor model and the dynamic response optimized by means of the Kuhn-Tucker method. A simulation study demonstrated that a sensor with a resolution of 15μ rad/s^2 and a bandwidth of 50 Hz can be packaged with a diameter of 22 mm and a height of 22 mm, when referenced against a noise level of $1\mu\mathrm{V}/\sqrt{\mathrm{Hz}}$.

Keywords: Angular motion, accelerometer, microfluidic, inertial navigation.

NOMENCLATURE

a	: speed of sound
α	: angular acceleration imposed on the channel in rad/s^2
α_k	: zeros of J_0
C_{amp}	: charge amplifier feedback capacitance
d	: wetted channel diameter in a fluid filled channel
d_{piez}	: piezo crystal charge sensitivity
E_{dia}	: Young's modulus of diaphragm material
J_0	: Bessel function of the first kind, zero order
J_1	: Bessel function of the first kind, first order
k_{pillar}	: combined stiffness of the piezo crystal and its supportive structure
k_s	: stiffness of the piezo crystal's support structure
K	: liquid bulk modulus

ΔP	: pressure difference
$\frac{dp}{dx}$	: pressure gradient
μ	: dynamic viscosity
ν	: kinematic fluid viscosity
ν_{dia}	: Poisson's ratio (not kinematic viscosity as in flow theory)
P	: differential pressure generated by the fluid-filled channel
ρ	: fluid density
$P(s)$	: Laplace transform of differential pressure over diaphragm
$Q(s)$	: Laplace transform of the flow
q	: applied differential pressure
t_{dia}	: diaphragm thickness
R_0	: diaphragm outside diameter
ΔV	: change in a volume of V liquid ("delta" not in Italics)
Vol_{dia}	: diaphragm volumetric deflection ("Vol" not in Italics)
y_b	: inner-edge deflection of the diaphragm

1. INTRODUCTION

Angular accelerometers are found on both sides of a performance and size divide. On the one side, large, accurate and expensive angular accelerometers are available. These accelerometers are designed as dedicated angular accelerometers from concept inception, and measure angular acceleration around one axis. The prime example of an angular accelerometer of this type utilizes the fluid rotor concept patented by Statham (1957) and is servoed. This sensor contains a torsionally suspended mass, rotated by paddles protruding into a toroidal fluid rotor. The concept is commercially available (although exports are controlled) and a resolution of 0.005% of full scale may be achieved. This transducer represents the present state of the art from a resolution point of view, but is in excess of 60 mm in length and 40 mm in diameter with a bandwidth in the region of 20 Hz. The second angular accelerometer falling in this category is the amorphic wire type described by Lassow and Meydan (1995). This type of sensor functions by causing torsional stress in the wire supporting the seismic mass, which in turn produces a Matteucci voltage over the clamps of the wire. A solenoid-magnetized, highly magnetostrictive, amorphous wire is required to obtain the voltage, which is modulated and measured. This concept has not found widespread use in industry, however, and is not as sensitive as the fluid rotor type.

The other side of the angular accelerometer divide is the domain of the micro-electro-mechanical system (MEMS) angular accelerometer. The common applications of this accelerometer are the stabilization of computer disk read/write heads and vehicle testing. These sensors are not as sensitive as the fluid rotor type, but are far smaller, cheaper and more diverse. Most linear accelerometer concepts can be converted to measure angular acceleration, which is a common strategy in MEMS angular accelerometers. MEMS angular acceleration sensors are not found in applications requiring high accuracy, however.

A literature study of contemporary angular accelerometry identified a niche for a high-sensitivity MEMS device. It is proposed that fluid inertia could be used more efficiently to achieve high angular acceleration sensitivity in a small package with suitable bandwidth for most inertial measurement applications, in this way countering the two main drawbacks of

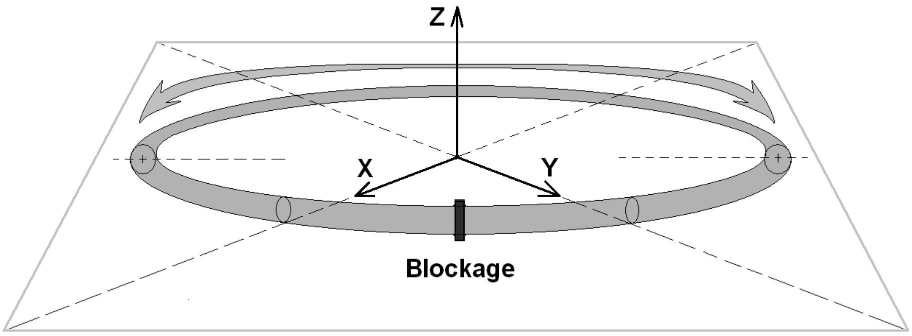

Figure 1. A toroid-shaped tube filled with liquid.

the fluid rotor angular accelerometer. The sensor must be insensitive to linear acceleration in any direction and to angular acceleration along the two non-sensitive angular axes. In an attempt to achieve such high sensitivity to angular acceleration, the Microfluidic Channel Angular Accelerometer (MFCAA) concept was used, as described in this article.

2. DESIGN CONCEPT

The MFCAA utilizes fluid inertia to measure angular acceleration. Fluid inertia in an acceleration field has the main effect of varying the pressure in the fluid, which in the MFCAA is transduced to a signal to provide a measure of angular acceleration.

Any constrained body of fluid undergoing a steady linear acceleration differing from that of the local gravity field (called the acceleration differential) eventually exerts a steady pressure in the fluid due to that acceleration. The pressure generated increases linearly in the direction of the linear acceleration differential to a maximum of $\rho a_{pot} h$, where h is the distance along the acceleration differential and ρ the fluid density. a_{pot} is the acceleration potential, and comprises the vector sum of the kinematic and gravitational accelerations. Because of this effect, linear accelerometers have no way of distinguishing between gravity and acceleration, but dedicated angular accelerometers ought not be significantly influenced by gravity. For this reason, the MFCAA does not measure absolute pressure; instead, it measures differential pressure.

A fluid-filled toroidal (circular and endless) tube is shown in Figure 1. The fluid, like the tube, is initially stationary. A blockage is also shown in the tube, preventing any flow inside. If there were no blockage or internal friction and the tube was rotated about its Z-axis as shown, the fluid inside the tube would remain stationary indefinitely. In such a case, flow would therefore be induced by the rotation of the tube. When there is a blockage present in the tube, any angular acceleration will cause the inertia of the fluid to generate a pressure. A high-pressure wave propagates at the fluid's speed of sound from the blockage in the direction of the angular acceleration, and a low-pressure wave propagates in the opposite direction at the same speed.

There is no immediate change in the pressure in the fluid at the far end of the tube when the motion begins. Eventually, the pressure waves will damp out due to various mechanisms, and exert a steady-state differential pressure at the blockage. This differential pressure is proportional to the applied acceleration. The difference in steady pressure across the blockage is a measure of the imposed steady angular acceleration on the tube. This is the operating principle of the MFCAA. The purpose of an MFCAA is to maximize the differential pressure generated across a diaphragm (channel blockage) by angular acceleration around the sensitive axis. The MFCAA is particularly well-suited to the requirement of cross-axis rejection because of its inherent rejection of any acceleration (angular or linear, including gravity) other than angular acceleration around the sensitive axis. Minor linear acceleration sensitivity is, however, experienced normal to the diaphragm, due to fluid compressibility and sensor height. The resulting output error will generally be negligible for most applications, or compensated for by measurement of the bias-causing acceleration.

The MFCAA changes the tubular loop shown in Figure 1 into a microfluidic channel forming a spiral-helix shape, which is optimized to generate maximum pressure from angular acceleration inputs. The channels are etched into wafers using micromachining techniques (or laser ablation), and then bonded to form the spiral helix. The channel array is assembled by stacking a series of two different types of wafer, which differ only in port position and the direction of the spiral. A spiral is used on each wafer to maximize the pressure generation, and a central area is left vacant for the measurement chamber. The top and bottom wafers have channels leading inward to feed the pressure measurement chamber. A narrower channel width allows a longer spiral and a thinner wafer, so that the total channel length increases in inverse proportion to the square of the channel width. The working fluid could be any fluid that is liquid in the sensor's temperature range. Mercury is particularly suitable owing to its high kinematic viscosity and low vapor pressure. A sectional view of the conceptual sensor is shown in Figure 2.

The pressure measurement chamber is shown containing the diaphragm and a baffle on either side. The baffle is intended to aid in keeping transient pressure waves out of the measurement chamber. Accumulators are shown at the top and bottom of the measurement chamber. The accumulator contains an elastic bladder, shown as a toroidal tube, which is filled with gas. The rest of the accumulator is filled with the working fluid and connected to the measurement chamber. The accumulator allows the thermal expansion of the working fluid and assists with the filling and pre-pressurization of the sensor.

3. PRESSURE GENERATION AND PROPAGATION

The angular pressure-generating potential of any channel is defined as

$$h_{ang} = \frac{P}{\rho\alpha} \tag{1}$$

where P is the differential pressure generated by the fluid-filled channel, ρ the fluid density and α the angular acceleration imposed on the channel in rad/s^2. h_{ang} has the unit m^2/rad. The potential is defined in this manner to keep the format the same as that for a straight

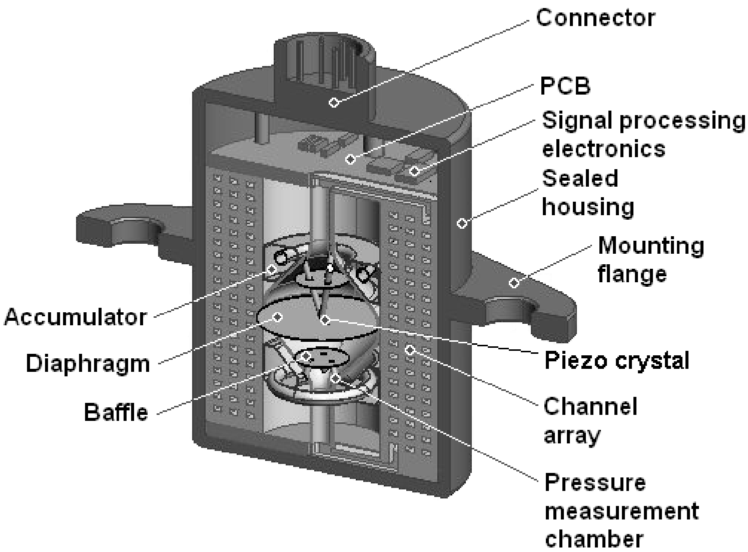

Figure 2. Section view of the sensor.

channel (which uses $P = \rho a_{pot} h$ as mentioned earlier) and so simplify the modeling of pressure generation.

The inherent compressibility of any fluid gives a finite wave propagation speed

$$a = \sqrt{\frac{K}{\rho}} \tag{2}$$

where ρ is the mass density and K is the liquid's bulk modulus. The bulk modulus defines the degree of compressibility in the liquid, and is given by

$$K = -\frac{\Delta P V}{\Delta V} \tag{3}$$

where a ΔP pressure variation causes a ΔV change in a volume of V liquid. The pressure propagation fundamentals of equations (1) to (3) are modeled using a discrete spring-mass multiple-degree-of-freedom (MDOF) model, shown in Figure 3.

The reasons for using a linear model are, firstly, rapid simulation for rapid optimization and, secondly, fast customization of the model to better predict sensor characteristics. Classic wave theory offers a feasible alternative to model wave propagation and computational fluid dynamics (CFD), for instance, can be used to model the fluid column. CFD would also consider all flow characteristics and thus make any need for further flow theory redundant. The CFD software would have to be able to simulate compressibility (wave propagation), in addition to flow, if the whole sensor model is to be included. Each optimization run would require its own solution convergence and if the optimization is to run independently

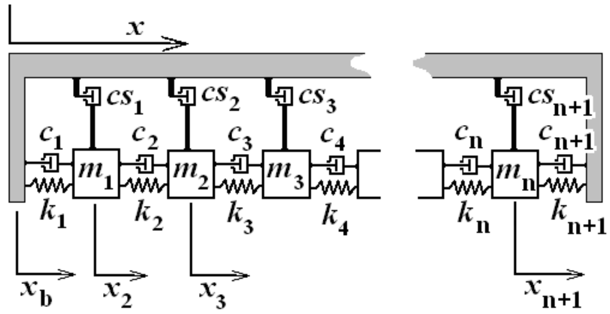

Figure 3. Discrete MDOF model of pressure propagation in a fluid column.

from user-input, many 3D models and meshes will have to be computer generated. Another limitation of contemporary CFD is the types of boundary conditions available, which do not yet include unsteady pressure inlets and outlets. CFD does provide a convenient method for determining a supplementary answer to the flow theory presented for the case of a step pressure input, however.

The MDOF model has rigid boundaries in order to model the fluid compressibility, caused by diaphragm deflection, separately from the fluid flow. The minute compressibility flow and the accompanying losses arising from fluid compressibility are modeled with fluid shear dampers. Viscous dampers model the intermolecular damping in the fluid column itself. The discrete model was coded in a state-space formulation that determined the differential pressure over a rigid diaphragm. The flow arising from the pressure differential was calculated subsequently, causing diaphragm deflection.

The speed of wave propagation predicted by an MDOF model depends on the model's fundamental frequency and becomes more accurate as the number of degrees of freedom (DoFs) of the discrete model increase. The frequency bands between successive resonances are also underestimated and increase similarly in accuracy with increasing number of DoFs. Code was written that adjusts the state-space model stiffness to a level simulating the true wave speed in the fluid. The number of resonances present for a discrete model is still finite, however, and the bands between resonances are still underestimated. This remaining error is managed by using the maximum possible number of DoFs permitted by computational power and matrix stability. Model integrity is tested, after the assembly of the other transfer functions in the sensor model, by verifying the system stability and matrix inversion condition, and making adjustments if necessary. For an inertial sensor, the frequency of interest is unlikely to exceed 150 Hz, which is therefore selected as the maximum frequency of interest. The pressure propagation model does not model the boiling of liquid (or cavitation) due to the low pressures generated, or the presence of free gas in the column. These two phenomena are undesirable in any case, and will be avoided in sensor design, construction and operation.

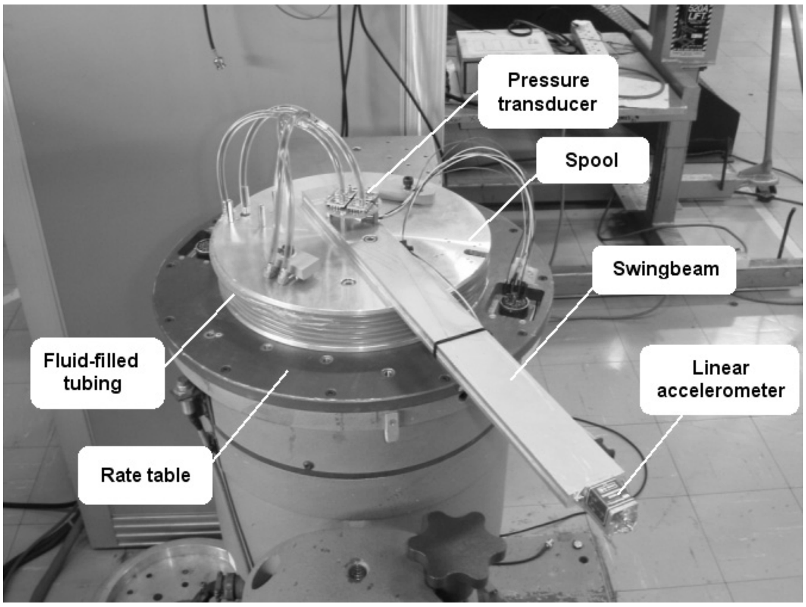

Figure 4. The rate tabletop with spool, PCB-mounted pressure sensors and wound tubing. The linear accelerometer is also shown at the end of the swingbeam.

4. EXPERIMENTAL VERIFICATION OF PRESSURE PROPAGATION THEORY

An experiment was conducted to confirm the validity of the pressure propagation model and to characterize a real fluid column under various conditions. A scaled-up version of the fluid column was constructed by winding 3 mm inner diameter polyurethane tubing around a 200 mm spool, as shown in Figure 4. Two absolute-pressure sensors mounted on an analogue printed circuit board were used to measure the pressures at the tube ends. The two measured pressures were separated, in order to better characterize the saturation in the pressure drop at the low-pressure end, and to detect free air in the column. The high ratio of tube area to the volumetric deflection of the pressure transducer makes the flow effects negligible, which approximates the rigid ends of the discrete fluid column model.

A rate table was used to impose the required angular accelerations on the spool. All signals and power were sent via slip rings and then sampled digitally at 2 kHz. A linear accelerometer was placed at the end of a swingbeam to measure angular acceleration. The integral of the accelerometer measurement was referenced to the internal tachometer speed output of the rate table, to verify the angular acceleration measurement. For safety reasons, diesel and water (instead of mercury) were used as the working fluid in the experiment. The high angular potential length of the tube (h_{ang} in equation 1) and the high motive power (angular acceleration) of the rate table compensated for the lower fluid density.

Great care was taken to remove all free air from the fluid column in the basic experiments. An additional experiment was conducted to investigate the effect of free air on the

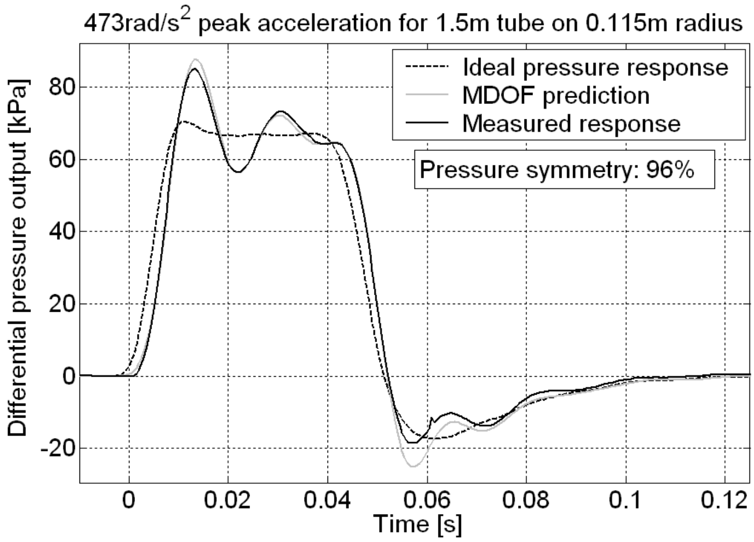

Figure 5. Test result for a 1.5 m long tube accelerated from rest to 900°/s in 50 ms. Applied acceleration in rad/s^2 is found by dividing the 'ideal pressure response' by 148.6 kg/(rad.m).

pressure propagation characteristics. When free air is present (even in small amounts), the pressures measured at the two ends of the tube become asymmetric. The symmetry of the two measured pressures is therefore a good measure of the quality of the fluid column. The compressibility of the free gas causes a greater oscillatory response than would be the case if no free gas were present. If smaller diameter channels were used, the compression of the free gas would cause greater flow and contribute to damping.

Two tubing systems were tested: a 20 m tube wound at a diameter of 220 mm and a shorter 1.5 m tube wound at 240 mm. The theoretical prediction compared with the measured pressures is based on a 51-DoF fluid column model. The physical properties of the tubing and working fluid are used to approximate the modified bulk modulus assumed for the fluid column model. Figure 5 presents the ideal pressure response (the pressure yielded by an incompressible fluid inside a rigid tube), plotted with both the measured and the predicted data. This imaginary pressure is directly proportional to the angular acceleration applied, and is included as a reference. The real pressure response will equal the ideal response in the steady state.

During the experimental runs, the spool was subjected to an impulsive acceleration up to a constant speed. The angular acceleration therefore decreases to zero. The result of one such experiment is shown in Figure 5. The results for the shorter tubing (shown) do not fit the predicted data as well as the results for the long tube do, because of the lower pressures involved and the more dynamic nature of the short tube's output. In fact, discerning measured output for the 20 m tubing from the predicted response is rather difficult. The pressure symmetry is also shown, as a measure of the quality of the fluid column used. These results confirm that a discrete MDOF model describes the dynamics of the fluid column sufficiently well for use in a simulation of the sensor.

5. FLOW IN CHANNELS

Due to the low flow and small channels in the sensor, the Reynolds numbers will also be small, and the flow laminar. By implication the flow speed will also be low; hence the flow may be considered incompressible. The flow will be unsteady, however, due to unsteady and arbitrary sensor input and the flow response to pressure feedback from a self-centering diaphragm. A numerical solution, via CFD in a time-marching scheme is possible, but requires massive computational power and coding to calculate results efficiently in an optimization routine. An analytical solution for the flow is more prudent for optimization that requires repeated runs. A round cylinder approximates the channel and any deviation from round is treated using the hydraulic diameter concept.

The unsteady flow profile in a cylindrical pipe arising from a step pressure input was first solved by Szymanski (1932). If the flow speed u is expressed as a function of time and radial co-ordinate r, the solution is given by Slezkin (1955) as

$$u\left(r,t\right) = -\frac{dp}{dx}\frac{d^2}{4\mu}\left[1-\frac{r^2}{d^2}-8\sum_{k=1}^{\infty}\frac{J_0\left(\alpha_k\frac{r}{d}\right)}{\alpha_k^3 J_1\left(\alpha_k\right)}\exp\left(-\alpha_k^2 Fo\right)\right] \tag{4}$$

where $\frac{dp}{dx}$ is the pressure gradient in Pa/m, ν the kinematic fluid viscosity, μ the dynamic viscosity and d the wetted channel diameter. J_0 and J_1 are Bessel functions of the first kind (zero and first order respectively) and α_k the zeros of J_0. $Fo = \frac{\nu t}{d^2}$ is called the Fourier number. Integrating equation (4) over the cross-sectional flow area to find volume flow yields

$$Q = \int_0^{2\pi}\int_0^{a} u(r,t)r\,dr\,d\theta = -\frac{dp}{dx}\frac{\pi a^4}{8\mu}\left[1-32\sum_{k=1}^{\infty}\frac{\exp\left(-\alpha_k^2 Fo\right)}{\alpha_k^4}\right]. \tag{5}$$

Equation (5) is not directly useful for simulating flow in a finite time-difference scheme, because a very large series will have to be solved for each time step. Another complication is that these equations are only valid for step pressure gradient inputs. The simulation may be required to handle many types of input in an optimization exercise.

An approach that readily suits any input shape is based on the concept of a transfer function, which provides the output of a process for any input. A transfer function is generally derived from first principles (according to the physics of the problem) by deriving an ordinary differential equation which contains the time derivatives of all relevant states. In the case of unsteady flow, a differential equation (namely the Navier Stokes equation) is already available, but unfortunately it is a partial differential equation which does not readily conform to Laplace transformation. Due to the difficulty of solving the Navier Stokes equation, the Bessel functions are employed to solve for the flow, and obtain equation (4). The flow rate given in equation (5) represents a time-based solution, to which a suitable transfer function could be fitted so that the flow can be properly simulated.

When considering the flow step response, with pressure used as the input, the response is close to that of a first order system. The main deviation occurs at the initial flow acceleration when the boundary layer develops at the outer edges of the cylinder. Theory has been derived which fits a first order response to flow that applies to a limited range of boundary layer development (Fourier number domain). A transfer function, general to a cylindrical channel of any dimension and pressure input, is

$$\frac{Q(s)}{P(s)} = \frac{\pi a^4/8\mu L}{\left(\frac{a^2\rho}{\mu 5.9925}\right)s + 1} \tag{6}$$

where $Q(s)$ and $P(s)$ are the Laplace transforms of the flow and differential pressure respectively. Equation (6) provides a formula fitted to the flow occurring across the whole Fourier number range, and is most accurate at Fourier numbers of 0.2.

6. PRESSURE TRANSDUCER

The type of pressure transducer may significantly influence sensor performance. There are various self-contained pressure sensors that can be fitted into a small volume. The piezo pressure transducer is a popular option, because of its superior stiffness and bandwidth. In the MFCAA, a piezo crystal is supported against the center of the diaphragm, where the maximum deflection would be for a plain diaphragm. Differential pressure on the diaphragm exerts a force and a small deformation of the crystal, producing a charge which is then amplified and conditioned. The main challenge when using the piezo transducer is its absence of DC response due to charge leakage. The time constant *(RC)* of the circuit results in a cutoff frequency, below which the response drops beneath 3dB. The cutoff frequency is managed mainly by using large feedback resistances in the charge amplifier of the piezo transducer. Increasing the feedback capacitance helps to increase the *RC* product, but also decreases sensitivity, which is why the focus remains on increasing resistance.

With the addition of the supported piezo crystal to the diaphragm, the deflection shape changes significantly from that of the plain diaphragm. Figure 6 shows various types of diaphragms for which analytical solutions were described by Young and Budynas (2002). A plain circular diaphragm deflection shape is shown in Figure 6a. The bottom two graphs in Figure 6 show an annular diaphragm at two extremes of operation. Figure 6b represents a diaphragm constrained by a rigid piezo crystal on the inside 20% of its diameter, applicable to a thin diaphragm and piezo crystal with stiff support. Figure 6c represents a diaphragm that is only guided to remain horizontal on its inner 20%, which applies to cases where the piezo support contributes negligible stiffness, but the diaphragm is unable to bend at the piezo crystal. Assuming that bending of the piezo crystal itself is negligible, and that it is mounted on a thick diaphragm with a relatively soft support, the deflection shape is approximately that given in Figure 6c. The true annular diaphragm of the piezo pressure transducer is a hybrid of Figures 6b and 6c. The stiffness of the diaphragm relative to its support dictates to what degree each extreme applies.

If the diaphragm deflection is less than half the diaphragm's thickness, the following formula is recommended for an annular diaphragm with a center support of finite stiffness:

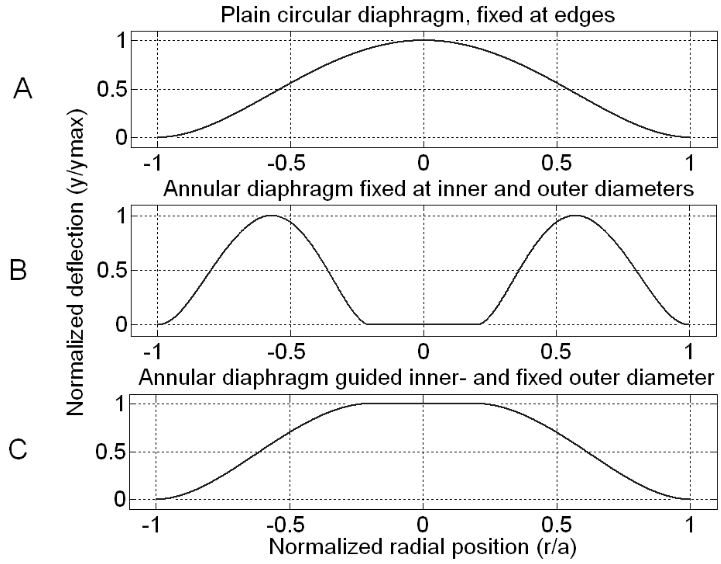

Figure 6. Deflection shapes of the plain circular diaphragm: (a) Annular diaphragm with both edges fixed, (b) annular diaphragm with a guided inner-edge, and (c) fixed outer diameter.

$$y_b = \frac{0.51274 q R_0^2}{k_{pillar} + \left(\frac{7.8214 E_{dia} t_{dia}^3}{R_0^2 (1 - \nu_{dia}^2)}\right)}. \tag{7}$$

Where q is the applied differential pressure and k_{pillar} is the combined stiffness of the piezo crystal and its supportive structure. y_b is the inner-edge deflection of the diaphragm and ν_{dia} is Poisson's ratio (not kinematic viscosity as in flow theory). For the diaphragm, E_{dia} is Young's modulus, t_{dia} the diaphragm thickness and R_0 the outside diameter. Equation (7) applies to a piezo element covering the innermost 34.6% of the diaphragm diameter. This ratio yields a maximum reaction force in the piezo support for the fixed-fixed diaphragm case, which is what the sensor design aims for.

The inner-edge deflection of this diaphragm, in terms of the volumetric deflection of the diaphragm, is

$$y_b = \frac{13.297 \, \mathrm{Vol}_{dia}}{R_0^4 \left(k_{pillar} + \frac{20.353}{R_0^2}\right)} \tag{8}$$

where Vol_{dia} is the diaphragm volumetric deflection.

7. SENSOR MODELING

The sensor model synthesizes the theory on the pressure generation, flow and pressure measurement into a model of the entire sensor; the three theory sections are designed to function

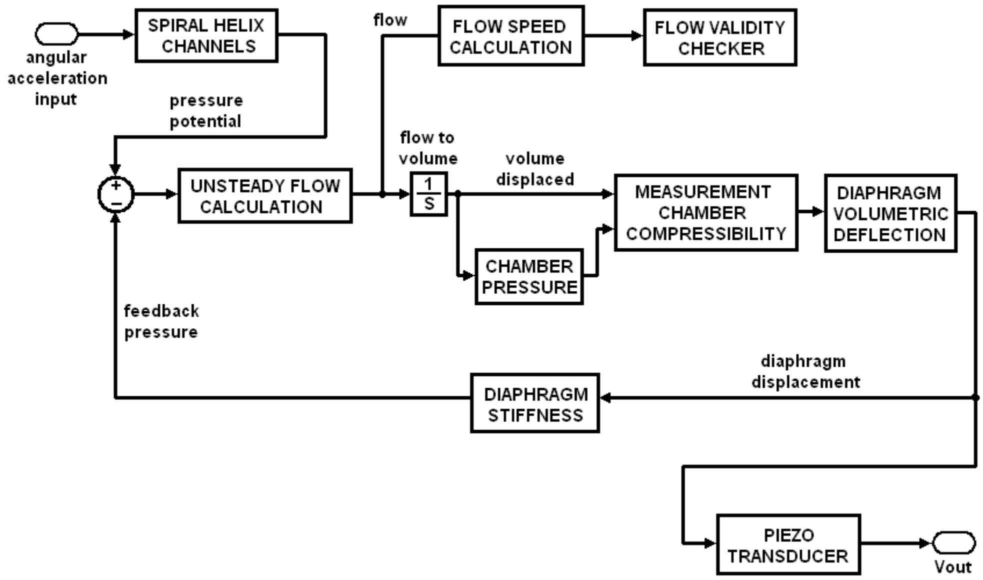

Figure 7. Sensor internal systems model architecture with cascaded pressure-to-flow loss model.

as separate contributions to the sensor frequency response. All contributions to the sensor performance have been modeled as linear transfer functions, allowing the theory to be integrated into a linear cascaded model of the sensor, as shown in Figure 7.

The sensitivity of the sensor can be determined without dynamic simulation. For a system with DC response, for example, sensitivity can be calculated by multiplication of steady state gains. The sensitivity of a piezo crystal cannot be calculated by multiplying DC gains, however, as a piezo crystal has no DC response. Piezo sensitivity is defined as peak output over peak input in the nominal sensitivity range. The nominal sensitivity range is above the RC cutoff point of the transducer and below the first resonance caused by the piezo crystal's interaction with its support structure. The sensor sensitivity in the nominal operating region of a piezo crystal is

$$\Theta_{piezo-nom} = \frac{0.51274 \rho h_{ang} R_0^2 d_{piez} k_s}{C_{amp}\left(k_{pillar} + \frac{7.8214 E_{dia} t_{dia}^3}{R_0^2\left(1-\nu_{dia}^2\right)}\right)} \tag{9}$$

where k_s is the stiffness of the piezo crystal's support structure, k_{pillar} is the combined stiffness of the support and piezo film and ν_{dia} is Poisson's ratio. d_{piez} is the piezo crystal charge sensitivity and C_{amp} is the charge amplifier feedback capacitance. As is often the case, equation (9) expresses a variable trade-off. No variable can be adjusted to give greater sensitivity without paying the price in the form of either a decrease in the dynamic performance or size of the sensor.

The model output is trimmed to create normalized Bode plots and step responses, according to the 0dB (nominal sensitivity) level given by equation (9). The diaphragm (or

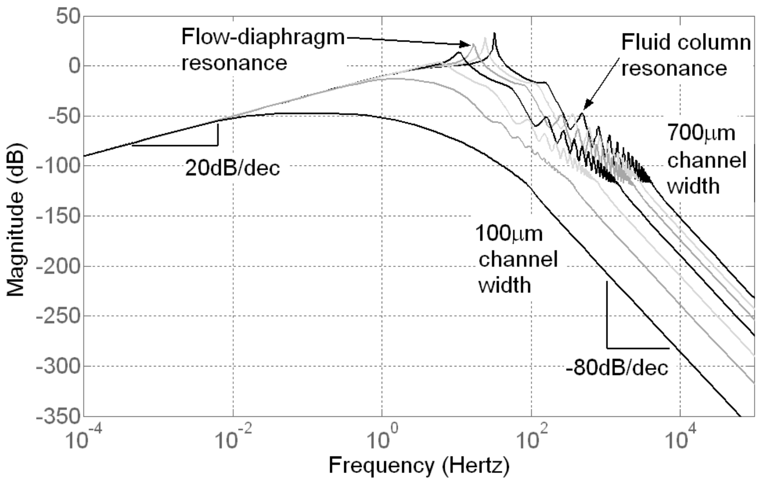

Figure 8. Bode plot showing the effect of increasing the channel width from 100 μm to 700 μm in equal increments. Channel length varies from 4.3 m for 700 μm channel width to 220 m for 100 μm channel width.

transducer) diameter, channel width and diaphragm thickness are the parameters that should be selected in a trade-off exercise. In cases where the pressure transducer becomes very small and all available space is used for the channel helix, the channel's inside diameter will be low, hampering pressure generation. In this case, the objective of maximum flow potential makes the inside diameter of the helix another variable to be optimized. Figure 8 shows a bode plot of a sensor with a 2 mm diameter diaphragm that is 500 μm thick, for various channel dimensions.

The response curve starts off with a 20dB-per-decade slope caused by the contribution of the piezo transducer. The response reaches its apex with the flow-diaphragm resonance and begins to decrease before the fluid column resonances start. The flow-diaphragm resonance is caused by the filling of the diaphragm's deflection volume by flow following a pressure differential. The position of the flow-diaphragm resonance (identified by a sharp phase drop) depends mainly on the diaphragm's stiffness and the ratio of channel cross-section area to diaphragm area. The position of the first fluid column resonance depends on the wave speed in the working fluid and the length of the fluid column. In a sensor with a long enough channel, the cascade of fluid column resonances may start at lower frequencies than the flow resonance. Due to the limited number of DoFs in the discrete model, not all of the fluid column resonances can be simulated. Each of the resonances represents one DoF of the fluid column and sensor body. The damping effect of decreasing channel width is clearly illustrated, and at 100 μm the large damping eliminates any sign of resonance.

The frequencies of the various resonances can be adjusted by selecting the design parameters carefully. The sensor displays a predominantly second-order response when the fluid column resonances are moved beyond the flow resonance by using a relatively short fluid column. This results in a monotonically increasing magnitude response to the first resonance, and a linearly decreasing phase response, which is desirable for most applications.

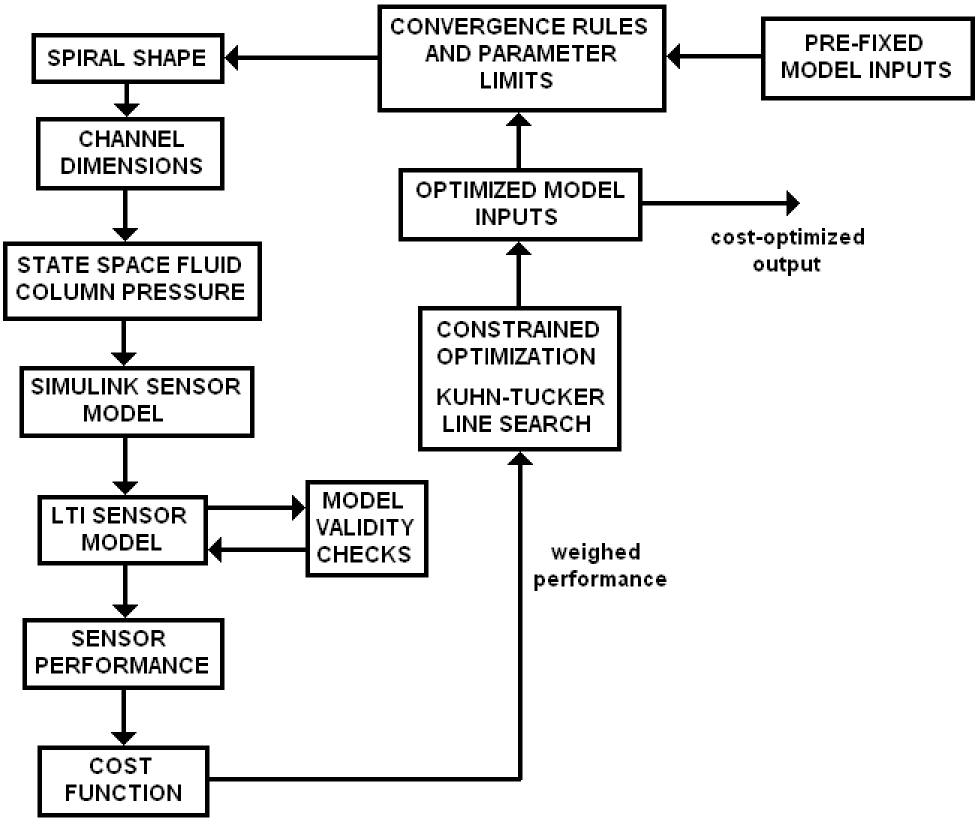

Figure 9. Schematic of the optimization method.

When using a long fluid column, the cascade resonances decrease in frequency and can be arranged to superimpose on the flow resonance. This results in a sensitive design with a less favorable frequency response.

8. SENSOR OPTIMIZATION

Sensor optimization was performed according to the Kuhn-Tucker line search method, applied to a set of inter-dependent sensor variables. A schematic of the simulation and optimization routine is shown in Figure 9.

Sensor performance was quantified using a cost function, according to a value system for what the designer perceived to be a suitable frequency response. This makes the method somewhat designer-subjective but allows a design to favor either a flat frequency response or high sensitivity and resolution. A generally accepted value system to pursue for a measurement system is: Resolution, flatness of magnitude response, linear phase response and input-output linearity. The optimization routine starts from user-selected initial conditions

Table 1. Constraints of optimization.

OPTIMIZATION CONSTRAINTS	Lower bound	Upper bound
Charge amp feedback capacitance	0.5 pF	100 F
Channel width	50 m	1 mm
Diaphragm thickness	50 m	1 mm
Diaphragm diameter	1 mm	9 mm

and converges to a solution if it exists. The sensitivity is referred to the 0dB level and is based on the nominal sensitivity of the piezo crystal. The nominal sensitivity and resolution are illustrative of the sensitivity attained at the quoted characteristics of the charge amplifier. Sensor resolution still depends greatly on the noise floor caused by various internal and external sources. The trade-off between the charge amplifier variables and noise must still be performed as part of the electronic design.

The optimization inputs must be constrained, because all the simulation inputs represent real sensor characteristics and, as such, are always positive real numbers with upper and lower bounds. This complicates the optimization method somewhat, because the routine requires a sufficient margin within which to calculate a finite difference approximation of a derivative. The bounds therefore have to be widened somewhat for the sake of the routine and results checked for feasibility afterwards. The optimization was commenced for a sensor outside diameter and sensor height fixed at 20 mm unless mentioned otherwise. Other limits were also imposed on the optimization routine, as noted in table 1.

Sensor simulation within these limits results in an elaborate function with many minima, when a cost function is applied. These multiple minima degrade the quality of the optimization result, because the routine tends to find only a local minimum and not the global minimum inside the optimization constraint limits. Various initial conditions therefore have to be tested to ascertain the quality of the result. Using an optimization routine exclusively for a design like this removes designer authority, and some fine-tuning therefore usually done around the ‘optimum’ result obtained by the routine.

The bulk of inertial applications require a bandwidth of approximately 50 Hz, which is where current MEMS vibrating-structure gyroscopes perform. This requirement can reach 100 Hz for missile applications. The following results assume a 0.5 pF charge amplifier feedback capacitance and 1TΩ feedback resistance, which results in a 0.318 Hz cutoff. In addition, $1\mu\mathrm{V}/\sqrt{\mathrm{Hz}}$ is taken as the amplifier noise benchmark for resolution calculation, since the noise spectra for contemporary charge amplifiers stay constant at this value up to almost 1 kHz. Figure 10 shows a response that increases monotonically inside the usable frequency range, with a bandwidth of 53 Hz. This is achieved by moving the fluid column resonances beyond the first flow resonance (see Figure 8). The phase response is of high quality and shows hardly any phase lag (5°) at 50 Hz. The $1\mu\mathrm{V}/\sqrt{\mathrm{Hz}}$ referenced resolution is below 15μ rad/s^2, which equals $8.59 \times 10^{-4\circ}/s^2$. With this sensitivity, a noise level of 50 mV (for the sensor as a whole) can be tolerated while still rivaling the 10^{-4} rad/s^2 accuracy of the angular accelerometers currently available. Since such a noise level is extremely high, a marked improvement may be expected as the state of the art progresses. If a longer fluid column is used, so that the column resonances move below the flow resonance, the sensitivity can be enhanced to 2μ rad/s^2, with an accompanying compromise that the column resonances will contaminate the magnitude flatness and phase linearity of the response. It is

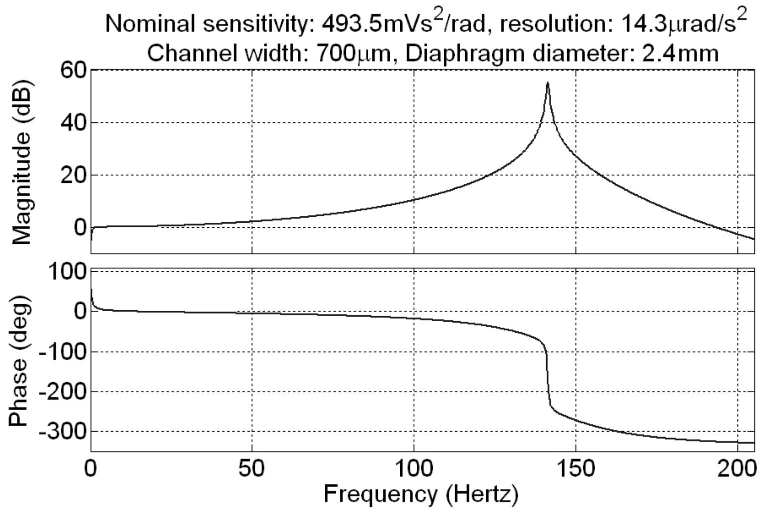

Figure 10. Bode plot of a design with monotone response inside the usable frequency range for a 20∅ × 20 mm wafer stack. Resolution is referenced against noise of $1\mu V/\sqrt{Hz}$.

preferable, therefore, to use a frequency range where the flow resonance is the first resonance peak, unless sensitivity is of the utmost importance. Another way of further improving the frequency response is by means of feedback inside the sensor, but this has not yet been studied.

The effect of sensor diameter on sensor performance is substantial. If the sensor wafer stack diameter is doubled (with no other changes), the sensor sensitivity is tripled for the same frequency response. If the sensor height is also doubled, the sensitivity can be quadrupled; the effect of sensor height is not as dramatic as that of sensor diameter. Decreasing the bandwidth requirement also allows better resolution. A sensor with 10 Hz bandwidth, which might be applied in gradiometers and satellites, has a $1\mu\mathrm{V}/\sqrt{\mathrm{Hz}}$ reference resolution of 4.8μ $\mathrm{rad/s}^2$. Reducing the bandwidth places further pressure on the cutoff frequency, which has to be decreased, in turn requiring higher charge amplifier feedback resistance. High resistance is difficult to obtain reliably and has noise implications.

9. CONCLUSIONS

A theoretical basis has been developed for the design and simulation of a novel microfluidic channel angular accelerometer. The proposed sensor consists of a central differential pressure transducer fed by a channel system in the shape of a spiral helix. The sensor model is comprised of separate theoretical building blocks for pressure generation, flow and pressure measurement, which are subsequently synthesized into a cascaded model.

Simulation studies indicate that the microfluidic channel angular accelerometer shows potential for the construction of a single-axis, solid-state angular accelerometer on the MEMS scale. This transducer may improve considerably on current MEMS technology in terms of sensitivity and stability, and fill a performance gap currently existing in miniature angular accelerometry. Other advantages offered by the concept of the microfluidic channel angular accelerometer are compactness, high shock resistance and design versatility. The main disadvantages are the number of elements in the assembly and the absence of a DC response when a piezo crystal is used in the pressure transducer. The bulk of the future work on the development of this sensor will be focused on the miniaturization of the pressure transducer and the design of its electronics.

REFERENCES

Statham, L. D., 1957, Angular Accelerometer, U.S. Patent #2,778,623.

Lassow, R. and Meydan, T., 1995, "Angular accelerometer using amorphous wire," *IEEE Transactions on Magnetics* **31(6, Part 1)**, 3179–3181.

Szymanski, P., 1932, "Quelques solutions exactes des équations de l'hydrodynamique du fluide visqueux dans le cas d'un tube cylindrique," (in French) *Journal de mathématique pures et appliqués*, **Series 9**. (Also in *Proceedings of the International Congress on Applied Mechanics*, Stockholm, Sweden).

Slezkin, N. A., 1955, *Dynamics of a viscous incompressible fluid*, (in Russian), Gostekhizdat, Moscow, Russia, pp. 325.

Young, W. C. and Budynas, R. G., 2002, *Roark's Formulas for Stress and Strain*, 7^{th} Edition, McGraw Hill, New York, pp. 466.